

## Structural and elemental influence from various MOFs on the performance of Fe@C catalysts for Fischer-Tropsch synthesis

Wezendonk, Tim A.; Warringa, Quirinus S E; Santos, Vera P.; Chojecki, Adam; Ruitenbeek, Matthijs; Meima, Garry; Makkee, Michiel; Kapteijn, Freek; Gascon, Jorge

**DOI**

[10.1039/c6fd00198j](https://doi.org/10.1039/c6fd00198j)

**Publication date**

2017

**Document Version**

Accepted author manuscript

**Published in**

Faraday Discussions

**Citation (APA)**

Wezendonk, T. A., Warringa, Q. S. E., Santos, V. P., Chojecki, A., Ruitenbeek, M., Meima, G., Makkee, M., Kapteijn, F., & Gascon, J. (2017). Structural and elemental influence from various MOFs on the performance of Fe@C catalysts for Fischer-Tropsch synthesis. *Faraday Discussions*, 197, 225-242. <https://doi.org/10.1039/c6fd00198j>

**Important note**

To cite this publication, please use the final published version (if applicable). Please check the document version above.

**Copyright**

Other than for strictly personal use, it is not permitted to download, forward or distribute the text or part of it, without the consent of the author(s) and/or copyright holder(s), unless the work is under an open content license such as Creative Commons.

**Takedown policy**

Please contact us and provide details if you believe this document breaches copyrights. We will remove access to the work immediately and investigate your claim.

## Structural and elemental influence from various MOFs on the performance of Fe@C catalysts for Fischer-Tropsch synthesis

Tim A. Wezendonk<sup>a</sup>, Quirinus S.E. Warringa<sup>a</sup>, Vera P. Santos<sup>b</sup>, Adam Chojecki<sup>b</sup>, Matthijs Ruitenbeek<sup>c</sup>, Garry Meima<sup>c</sup>, Michiel Makkee<sup>a</sup>, Freek Kapteijn<sup>a</sup> and Jorge Gascon<sup>a</sup>

Received 00th January 20xx,  
Accepted 00th January 20xx

DOI: 10.1039/x0xx00000x

www.rsc.org/

The structure and elementary composition of various commercial Fe-based MOFs used as precursors for Fischer-Tropsch synthesis (FTS) catalysts have a large influence on the high-temperature FTS activity and selectivity of the resulting Fe on carbon composites. The selected Fe-MOF topologies (MIL-68, MIL-88A, MIL-100, MIL-101, MIL-127, and Fe-BTC) differ from each other in terms of porosity, surface area, Fe and heteroatom content, crystal density and thermal stability. They are reengineered towards FTS catalysts by means of a simple pyrolysis at 500 °C under N<sub>2</sub> atmosphere and afterward characterized in terms of porosity, crystallite phase, bulk and surface Fe content, Fe nanoparticle size and oxidation state. We discovered that the Fe loading (36-46 wt%) and nanoparticle size (3.6-6.8 nm) of the obtained catalysts are directly related to the elementary composition and porosity of the initial MOFs. Furthermore, the carbonization leads to similar surface areas for the C matrix ( $S_{\text{BET}}$  between 570-670 m<sup>2</sup> g<sup>-1</sup>), whereas the pore width distribution is completely different for the various MOFs. The high catalytic performance ( $FTY$  in the range of 1.9-4.6 · 10<sup>-4</sup> mol<sub>CO</sub> g<sup>-1</sup> Fe s<sup>-1</sup>) of the resulting materials could be correlated to the Fe particle size and corresponding surface area, and only minor deactivation was found for the N-containing catalysts. Elemental analysis of the catalysts containing deliberately added promoters and inherent impurities from the commercial MOFs revealed the subtle interplay between Fe particle size and complex catalyst composition in order to obtain high activity and stability next to a low CH<sub>4</sub> selectivity.

### Introduction

Fischer-Tropsch synthesis (FTS) is a process that catalytically converts syngas, a mixture of CO and H<sub>2</sub>, towards longer chain hydrocarbon products such as gasoline, diesel and plastics precursors. The FTS process was designed nearly a century ago to cope with the limitations in petroleum feedstock, allowing the production of fuels and chemicals from coal, natural gas and biomass<sup>1-2</sup>. Currently, several large plants worldwide operate the FTS process through syngas obtained from steam methane reforming or coal gasification<sup>3-6</sup>. Fast-growing worldwide energy consumption and conventional oil reserve challenges provide a continuous drive to develop improved catalysts for the FTS process.

Since a few years, metal-organic frameworks (MOFs) have emerged from the deep waters of scientific research and have been proposed increasingly as heterogeneous catalysts for many applications, such as Knoevenagel condensation, “click” chemistry, selective hydrogenations, Friedländer coupling, electrocatalysis and photocatalysis<sup>7</sup>. However, we have

showed recently that MOFs are not only potent catalysts in their final form, but they also serve the purpose as excellent precursors for high-temperature FTS (HTFTS) catalysts<sup>8</sup>. The concept of the synthesis technique is a simple pyrolysis, heat treatment in an inert atmosphere, which carbonizes the MOF towards embedded metal nanoparticles in a porous C matrix (M@C). The resulting nanoparticle-carbon composites possess outstanding properties for application in electrodes, electrocatalysts and H<sub>2</sub>/CO<sub>2</sub> adsorbents<sup>9-13</sup>; these materials amongst many others have been comprehensively reviewed<sup>14</sup>. Recent investigations into MOF-derived catalysts for FTS by the group of Wang confirmed the high potential of the Fe@C system using the MIL-88B topology as catalyst precursor<sup>15</sup>. Recently, we reported an in-depth study of the nature of the Fe species during pyrolysis and subsequent FTS reaction, elucidating the carbonization mechanism of the commercial Fe-BTC MOF with the MIL-100 topology<sup>16</sup>. *In situ* DRIFTS-MS and XAFS applied during the pyrolysis process revealed the decarboxylation of the framework and auto-reduction of the Fe<sup>3+</sup> species towards active Fe carbide. *In situ* Mössbauer emission spectroscopy and HR-TEM allowed for the correlation of the pyrolysis temperature and the Fe nanoparticle size and showed the evolution of the Hågg carbide phase depending on the particle size as the FTS reaction progressed.

Herein, we determine how the MOF topology is related to activity and selectivity in HT-FTS in order to optimize the Fe@C catalyst. By systematically varying the structure and elemental

<sup>a</sup> Catalysis Engineering, ChemE, Delft University of Technology, Van der Maasweg 9, 2629 HZ Delft, The Netherlands.

<sup>b</sup> Core R&D, <sup>c</sup> Hydrocarbons R&D, Dow Benelux B.V., P.O. Box 48, 4530 AA, Terneuzen, The Netherlands.

Electronic Supplementary Information (ESI) available: Additional MOF identification, Fe@C characterization, FTS results and spent catalyst results. See DOI: 10.1039/x0xx00000x

composition prior to pyrolysis, we gain understanding in the transformation of the framework towards an active Fe@C catalyst. The commercially available Fe-MOFs selected in this study (MIL-68, MIL-88A, MIL-100, MIL-127, MIL-101-NH<sub>2</sub> and Fe-BTC) comprise carboxylate linkers that differ both in size and connectivity, in addition to heteroatoms such as N. Therefore, the MOFs show large differences in porosity, thermal stability and heteroatom content, summarized in Table 1 and Figure 1. The size of the biggest voids within these structures ranges from 6 to 34 Å with corresponding BET areas between 40-4100 m<sup>2</sup> g<sup>-1</sup>. The thermal stability in air, depending on the strength of the metal-ligand interaction, varies between 200-360 °C. We deliberately assess the use of commercial MOFs as a route towards industrial catalyst manufacturing. Several MOF producers exist nowadays (e.g. MOF Technologies, NuMat Technologies, The MOF Company, all spin-off companies from academia<sup>17-20</sup>), each using different manufacturing technologies, bearing an aspect that is to be investigated. Prices of MOFs are expected to come down and more focus on industrial scale production increases the chances on industrial implementation of MOFs.

## Results

### Characterization of MOF precursors

N<sub>2</sub> physisorption at 77 K, TGA and XRD confirmed the presence of MIL-68<sup>21-23</sup>, MIL-88A<sup>24-26</sup>, MIL-100<sup>27-29</sup>, MIL-101<sup>30-32</sup>, and MIL-127<sup>33-35</sup> (see Table S1, Figure S1 and Figure S2)†. XRD of the F300 Fe-BTC MOF revealed a very low degree of crystallinity, but the MIL-100 topology was confirmed since the isotherm contained an additional step in the micropore regime corresponding to the large cages in the MTN-type framework<sup>27-28</sup>. This behaviour was more pronounced in the MIL-100 sample, and values for porosity exceeded the F300 as well. As reported, MIL-88A heavily contracts upon degassing and thus, a near-zero N<sub>2</sub> uptake was found<sup>23-24</sup>. In general, no significant deviation from literature values was found.

### Characterization of Fe@C catalysts

**Texture of C matrix and crystalline Fe phases.** N<sub>2</sub> physisorption at 77 K of the Fe@C materials showed highly microporous catalysts with significant contributions of mesopores and external surface area (Table S2 and Figure 2a). To estimate the porosity of the C matrix, these values were

Table 1. Fe-MOF properties taken from reported literature studies<sup>21-35</sup>, comprising BET area ( $S_{BET}$ ), Fe loading ( $w_{Fe}$ ), calculated crystal density ( $\rho_{cryst}$ ), pore diameter ( $d_{pore}$ ) and decomposition temperature in air ( $T_d$ ).

Fe-based MOF	$S_{BET}$ m <sup>2</sup> g <sup>-1</sup>	$w_{Fe}$ %	$\rho_{cryst}$ g cm <sup>-3</sup>	$d_{pore}$ Å	$T_d$ °C
MIL-68	355	23.6	0.87	6-16	290
MIL-88A	40	26.2	1.55	6	195
MIL-100	2150	25.8	0.69	25-29	300
MIL-101-NH <sub>2</sub>	4100	22.5	0.62	29-34	320
MIL-127	1400	21.3	0.97	6-10	360
F300 Fe-BTC	1040	25	na	22	295

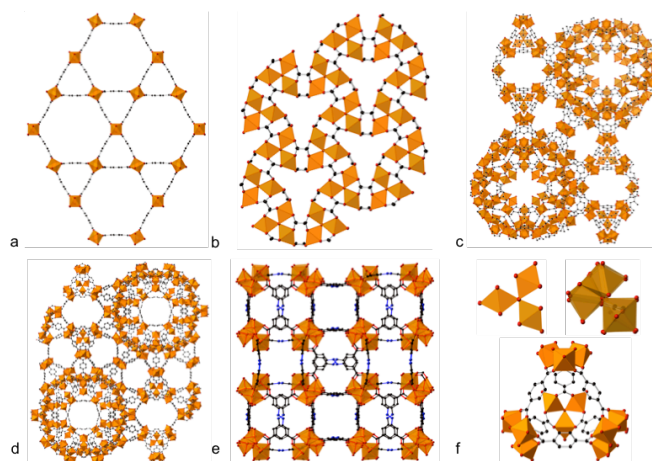


Figure 1. Selected Fe-MOF topologies: a) MIL-68 b) MIL-88A c) MIL-100 d) MIL-101 e) MIL-127 and f) the configuration of Fe trimers and super tetrahedra present in the different structures.

normalized on the C content correcting for the Fe mass assuming a Fe<sub>2</sub>O<sub>3</sub> phase (Table 2). The resulting BET areas are closely aligned, with the lowest value of 570 m<sup>2</sup> g<sup>-1</sup> for the low-crystalline starting MOF Fe-BTC. It is clear that the coordinated solvent molecules located in the intra-framework sites (MIL-68, MIL-88A) are released during the carbonization, liberating the MOF porosity. In the specific case of MIL-88A, which is not porous prior to pyrolysis, the pore volume is increased to 0.47 cm<sup>3</sup> g<sup>-1</sup> of C matrix with corresponding BET area of 655 m<sup>2</sup> g<sup>-1</sup>. This is an impressive result, especially keeping in mind that these values are one third of carbonized ZIF-8 at 800 °C<sup>10</sup>. Although values derived from the BJH pore size distribution have to be taken as merely qualitative, clear trends can be obtained from this analysis (Figure S3). The MIL-68 derived material, Fe@C-MIL68, contains most of its pore volume in large meso-macropores of around 50 nm in size, whereas for the Fe@C-MIL100 and -127 well-defined mesopores exist in a narrow distribution between 10-20 nm in addition to the micropores. XRD results demonstrated that nanocrystalline Fe oxides ( $\gamma$ -Fe<sub>2</sub>O<sub>3</sub>) were formed for Fe@C-MIL68, -88, -100 and -F300 after passivation of the material (Figure 2b). However, the diffraction pattern of Fe@C-MIL127 revealed the presence of a single Fe carbide phase (cementite), without Fe oxide phases present. MIL-127 possesses the lowest amount of Fe, although the C/Fe ratio is similar to that of MIL-68 and MIL-101NH<sub>2</sub>, suggesting that either the N functionality or the high decomposition temperature play a role in the carburization of Fe during the pyrolysis.

**Bulk and surface Fe loading.** TGA and ICP analyses were performed to determine the bulk Fe loading of the pyrolyzed MOFs, establishing values between 36-46 wt% of Fe (Table 2 and Figure S5). Both techniques suggest a nonlinear relation between the Fe loading of Fe@C and initial Fe-MOF loading. Only Fe@C-MIL100 shows an unexpectedly large deviation between TGA and ICP results, indicating that non-C impurities can be present. Elemental analysis of Fe and C allowed for the calculation of the remainder phase, assumed as O (Figure 3a).

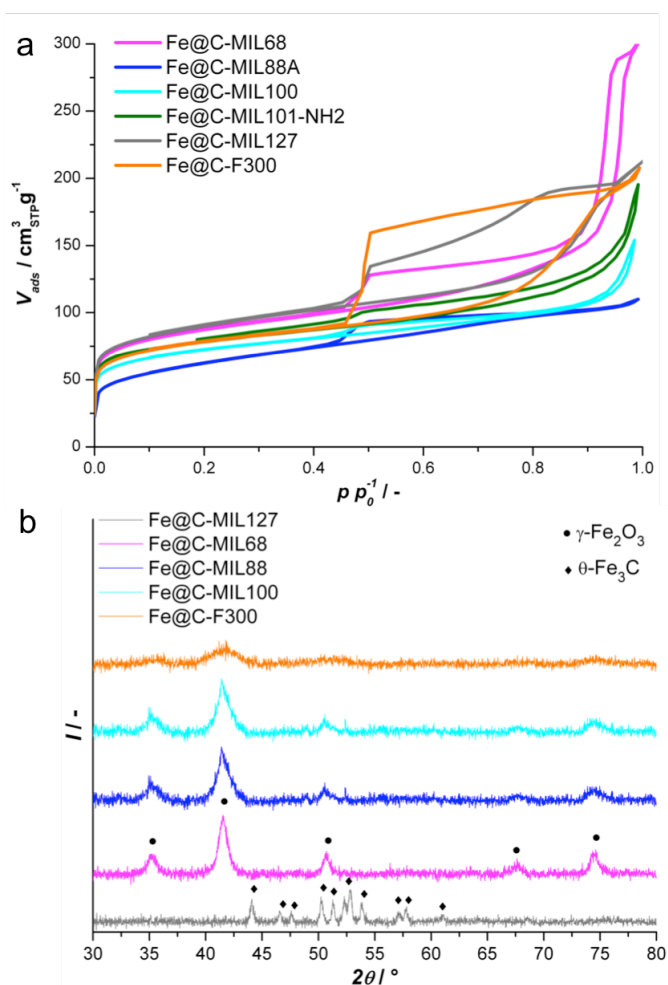


Figure 2. a) Nitrogen uptake at 77 K per gram of Fe@C catalyst and b) XRD of the Fe@C catalysts, indicating the presence of nanosized  $\gamma$ - $\text{Fe}_2\text{O}_3$  and  $\theta$ - $\text{Fe}_3\text{C}$  phases present after passivation.

By accounting for the Fe loading and associated O content as  $\text{Fe}_2\text{O}_3$ , we calculated the C/O ratio of the matrix in order to estimate the degree of carbonization (Table 2). Remarkably, for all the different MOFs, except for MIL-127, the mass balance of the leaving groups is  $\text{CO}_2 + (\text{H}_2)\text{O}$ , indicating a very similar degree of carbonization. On the other hand, the decomposition mass balance for MIL-127 suggests the release of only 2 ( $\text{H}_2$ )O and no  $\text{CO}_2$  upon carbonization, thus confirming the higher C content in this particular pyrolyzed

Table 2. Fe@C properties determined by ICP (Fe loading and O-functionalization of C,  $w_{\text{Fe}}$  and C/O), XPS (Fe surface/bulk ratio  $\text{Fe}/\text{Fe}$  S/B),  $\text{N}_2$ -physisorption (BET area,  $S_{\text{BET}}$ ) and HR-TEM (average particle diameter,  $d_{\text{Fe}}$ ).

Catalyst	$S_{\text{BET}}$ $\text{m}^2 \text{g}^{-1}$	$w_{\text{Fe}}$ %	C/O (bulk)	$\text{Fe}/\text{Fe}$ (S/B) %	$d_{\text{Fe}}$ nm
Fe@C-MIL68	675	37.3	6.9	31	6.8
Fe@C-MIL88A	655	46.1	3.3	55	5.9
Fe@C-MIL100	610	38.1	2.8	53	4.2
Fe@C-MIL101NH <sub>2</sub>	635	39.8	na	na	4.2
Fe@C-MIL127	585	34.5	3.9-0.5N	4	4.3
Fe@C-F300	570	35.7	4.2	50	3.6

MOF. Furthermore, the C/O/N ratio suggests that either the N=N bond is maintained, or scission followed by incorporation into the C has taken place. XPS analysis showed that the encapsulation of Fe by the C matrix varied greatly between 45-96% (Figure 3b) and that the Fe content at the exposed Fe@C surface is a linear function of the Fe loading of the MOF. Interestingly, the surface of Fe@C-MIL127 consists almost exclusively of N-functionalized C, with only 1.3 wt% Fe on the surface. Fe@C-MIL100 and -F300 contain nearly the same fraction of Fe on the surface, in addition to a very similar bulk Fe loading.

**Fe oxidation state and C matrix functionalization.** Fe core-level XPS spectra illustrated that the Fe surface consists mainly of  $\text{Fe}_2\text{O}_3$ , as witnessed by the binding energy of 710.9 eV for the  $2p_{3/2}$  peak and multiplet splitting with satellite features due to the high spin  $\text{Fe}^{3+}$  phase<sup>36</sup>. These findings indicate that the  $\theta$ - $\text{Fe}_3\text{C}$  phase of Fe@C-MIL127 is covered by a protective oxide layer, most likely formed during the passivation of the sample, implying that the Fe surface is at least partially

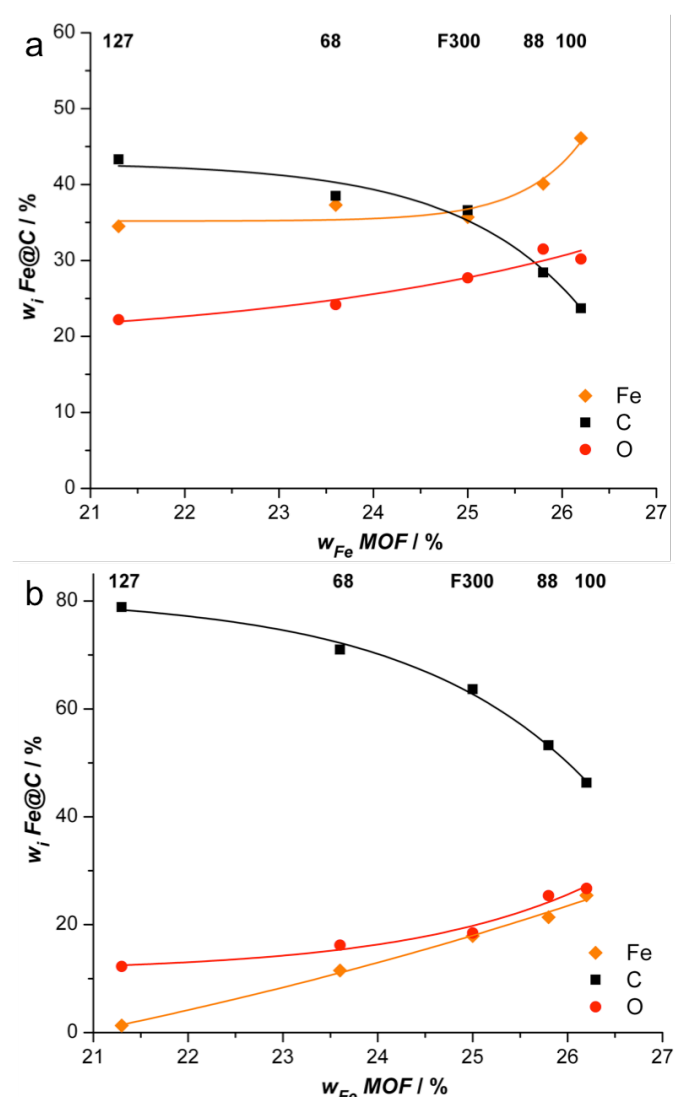


Figure 3. a) Bulk and b) surface Fe@C catalyst composition as function of Fe loading of parent MOF calculated from ICP and XPS, respectively.

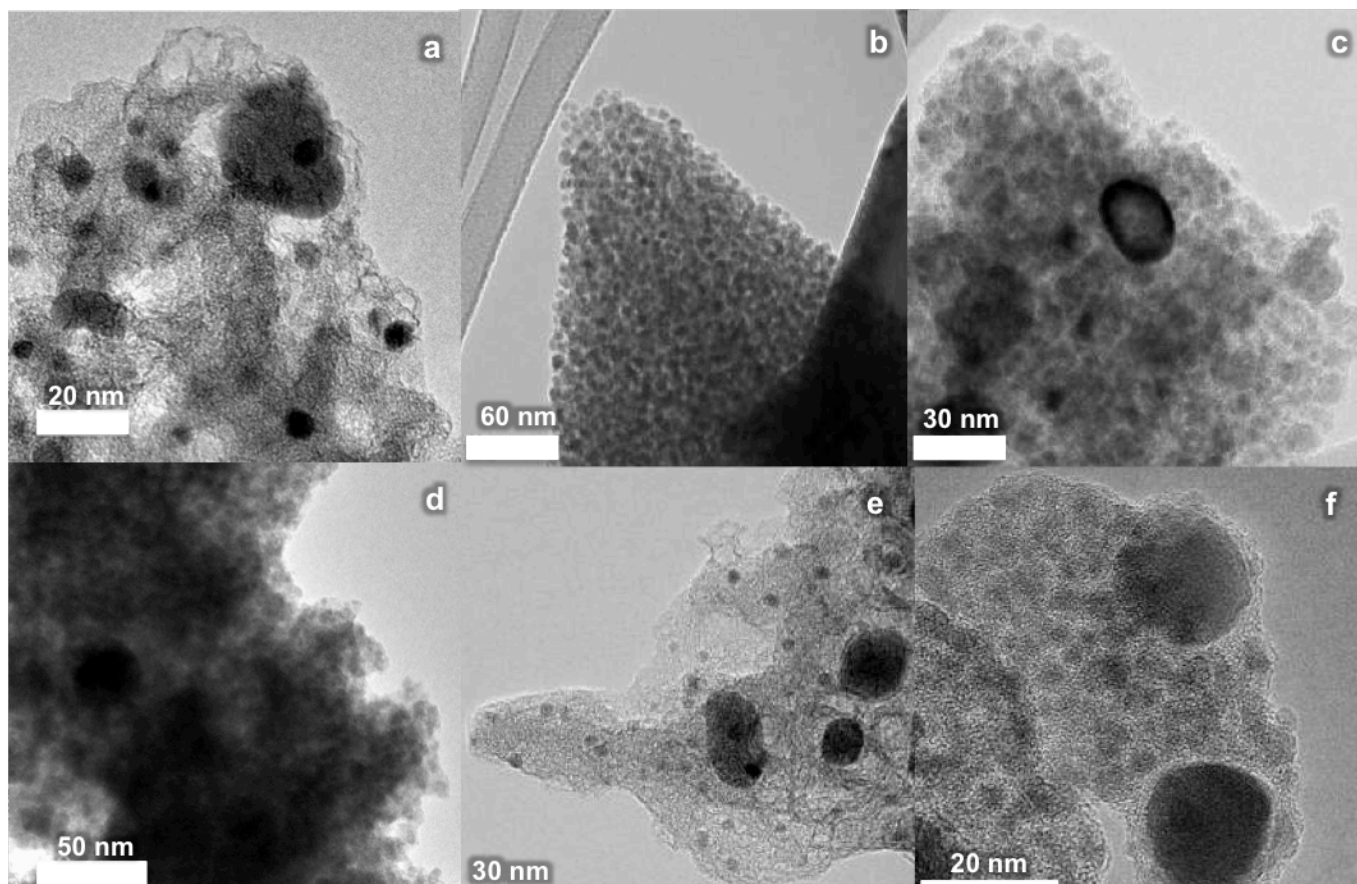


Figure 4. TEM images of a) Fe@C-MIL68, b) Fe@C-MIL88, c) Fe@C-MIL100, d) Fe@C-MIL101NH<sub>2</sub>, e) Fe@C-MIL127 and f) Fe@C-F300. Small Fe nanoparticles (medium contrast spheres) can be distinguished from the carbonaceous matrix (higher transmission), and are often accompanied by a number of agglomerates (large spheres). The high dispersion is still visible in larger fragments where several layers of particles overlap.

accessible. The XPS survey spectra were used to calculate the degree of O-functionalization of the C surface by accounting for the Fe loading and accompanied O content (Figure 3b). We can divide the catalysts into high- and low degree of O-functionalized carbons, with Fe@C-MIL88 and -100 containing between 23 and 26 O atoms per 100 C atoms, and Fe@C-MIL68, -127 and -F300 only 11 to 13 O atoms per 100 C atoms. Additionally, the surface of the C matrix of Fe@C-MIL127 was found to contain 9 N atoms per 100 C atoms, and 3 contributions could be distinguished from the N core-level spectra. The binding energies of the peaks are located at 398.7, 399.4 and 400.4 eV, demonstrating the presence pyrrolic, pyridinic and graphitic N species<sup>37-38</sup>. The surface N content was even higher in comparison to the bulk value, 7.1 wt% versus 5.6 wt%, respectively. Furthermore, the survey spectra exposed the presence of impurities in addition to the expected Fe, C, O and N contributions. Additional N signals were obtained from the spectra of Fe@C-MIL68 and -100, but were below 0.5 wt%. Both Fe@C-MIL88 and -127 contained significant amounts of Cl (1.5 and 1.0 wt%, resp.), possibly originating from the FeCl<sub>3</sub> reactant in the synthesis process. Fe@C-MIL100 contained a large amount of Cr and Mo surface

impurities (both 2.8 wt%), which explains the large deviation between the Fe loading obtained from ICP and that calculated from TGA analysis (~7 wt%). The higher bulk content of these metal impurities suggests that they are not encapsulated by C, affirming the origin of the impurities in the MOF synthesis.

**Morphology and Fe particle size.** SEM analysis illustrates the conservation of the MOF morphology after pyrolysis, showing large differences in the crystallinity and grain size (Figure S6). However, the maximum size of the crystallites did not exceed a few micrometer, and thus we expect no diffusion limitations in the HT-FTS performance of the various Fe@C catalysts. TEM images (Figure 5 and S8) were analysed to calculate the average Fe nanoparticle size (Table 2) and to generate particle size distributions (PSD) of the Fe@C catalysts (Figure S7). The average particle size, excluding the agglomerate fraction, was estimated between 3.6-6.8 nm. The PSDs show that the majority of the particles are below 10 nm, implying a homogeneous carbonization of the framework towards the embedded Fe on C system. No dependence of the Fe loading on the Fe particle size exists, much contrary to conventional catalyst synthesis routes.

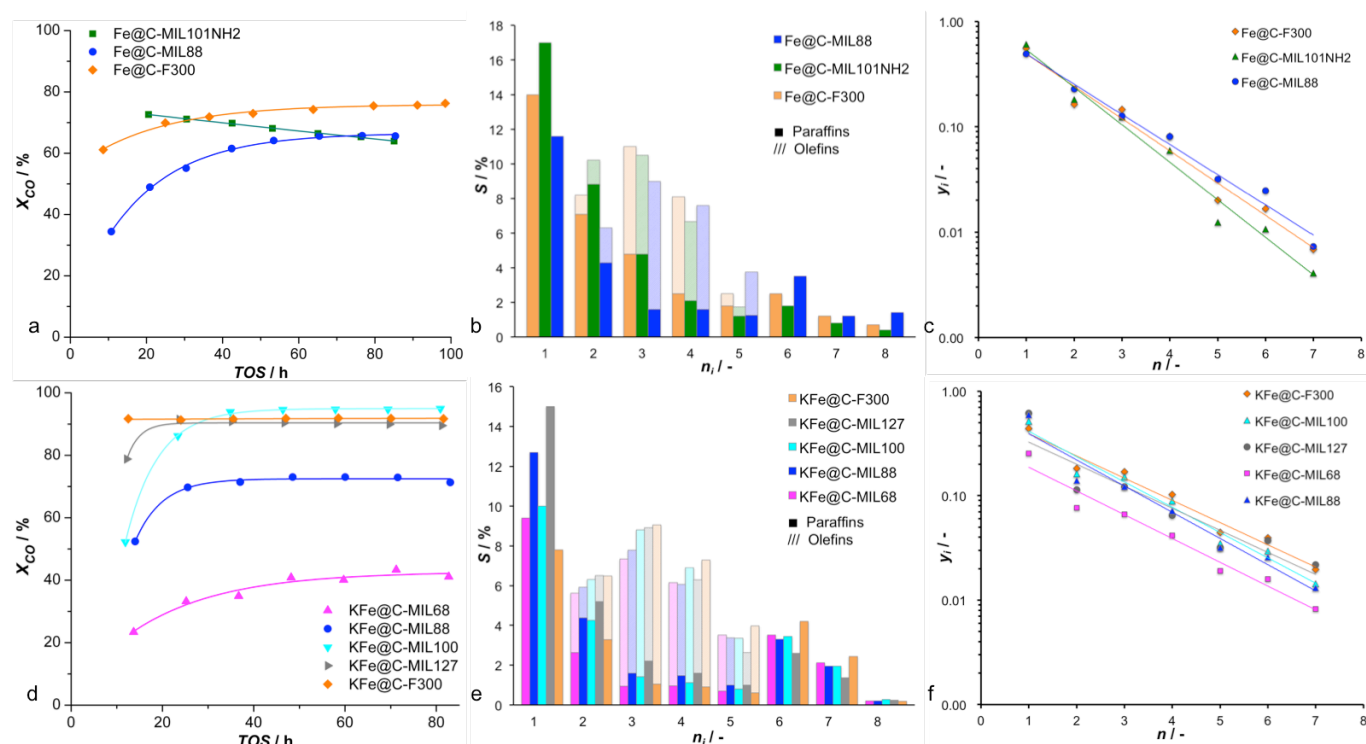


Figure 5. HT-FTS performance of a-c) unpromoted and d-f) K-promoted Fe@C catalysts, displaying CO conversion levels versus time on stream, C-based selectivity with product distributions and Anderson-Schulz-Flory plots to assess the chain growth probability. Reactions were carried out at 340 °C, 20 bar, H<sub>2</sub>/CO = 1 and employing a space velocity of 15 cm<sup>3</sup> syngas g<sup>-1</sup> cat s<sup>-1</sup>. Product analysis of the unpromoted and promoted catalysts was carried out at steady state conversion after 80 h time on stream (TOS). Paraffin and olefin selectivity is lumped from C<sub>8</sub> onward.

**K-promotion of Fe@C catalysts.** Elemental analysis confirmed that the targeted promotor loading of 0.6 wt% K was obtained for the Fe@C catalysts values varying from 0.53 to 0.59 wt%. EDX mapping confirmed the high dispersion of the promotor throughout the bulk phase of the catalysts. K2p core-level contributions were confirmed in the tail of the C1s core-level XPS spectra.

#### Catalytic testing

**Unpromoted Fe@C catalyst performance.** Previous results had shown improved activity and product selectivity for K-promoted Fe@C catalysts<sup>8</sup>, however, 3 unpromoted samples were tested in HT-FTS as well; Fe@C-MIL88, -101NH<sub>2</sub> and -F300 (Figure 5). Although Fe@C-MIL101NH<sub>2</sub> showed the highest activity after 20 h ( $X_{CO} = 72.6\%$ ), a linear deactivation rate resulted in the lowest CO conversion after 80 h. Fe@C-MIL88 and -F300 displayed an activation period over 50 h after which the CO conversion levels stabilized. Fe@C-MIL88 exhibited lower CH<sub>4</sub> selectivity levels than Fe@C-F300, whereas Fe@C-MIL101NH<sub>2</sub> reached a value over 17%. This catalyst additionally produced the lowest O/P ratios over the entire product slate, combined with the lowest value for the

chain growth probability ( $\alpha = 0.43$ ). These results are indicative of increased hydrogenation, possibly by enhanced readsorption of unsaturated hydrocarbons by the N-functionalized C. The enhanced hydrogenation might also explain the significant deactivation, as CO methanation is far more exothermic than Fischer-Tropsch ASF-type hydrocarbon production ( $\Delta H_f^0 = -247$  kJ/mol<sub>CO</sub> vs  $-177$  kJ/mol<sub>CO</sub> for  $\alpha = 0.5$ , respectively<sup>39-40</sup>). Fe@C-MIL88 displayed the highest  $\alpha$ -value of 0.54, while Fe@C-F300 obtained the highest activity ( $FTY = 3.78 \cdot 10^{-4}$  mol<sub>CO</sub> g<sup>-1</sup> Fe s<sup>-1</sup>).

**K-promoted Fe@C catalyst performance.** In general, and in good agreement with the literature<sup>41-42</sup>, the potassium promotion of the catalysts resulted in a significant increase in CO conversion, decrease in methane selectivity, increased O/P ratios and higher values for  $\alpha$  in the HT-FTS experiments (Figure 5). However, large differences in the CO conversion levels for the different KFe@C catalysts are observed, as KFe@C-MIL68 and -88 convert significantly less CO and consequently, their  $FTY$  values are the lowest. KFe@C-MIL100 and -F300 display very similar CO conversion and  $FTY$ , though

Table 3. Catalytic performance of unpromoted Fe@C catalysts.

Catalyst	$X_{CO}$ %	$FTY$ 10 <sup>-4</sup> mol <sub>CO</sub> g <sup>-1</sup> Fe s <sup>-1</sup>	$S_{CH_4}$ %	$S_{CO_2}$ %	$\alpha$ -
Fe@C-MIL88	66	2.59	11.6	46	0.54
Fe@C-MIL101NH <sub>2</sub>	65	2.90	17.2	47	0.43
Fe@C-F300	76	3.73	14.0	47	0.48

Table 4. Catalytic performance of K-promoted Fe@C-catalysts.

Catalyst	$X_{CO}$ %	$FTY$ 10 <sup>-4</sup> mol <sub>CO</sub> g <sup>-1</sup> Fe s <sup>-1</sup>	$S_{CH_4}$ %	$S_{CO_2}$ %	$\alpha$ -
KFe@C-MIL68	41.1	1.86	9.4	55	0.60
KFe@C-MIL88A	71.3	2.62	12.7	49	0.58
KFe@C-MIL100	94.9	4.23	10.0	47	0.56
KFe@C-MIL127	89.5	4.46	15.0	49	0.65
KFe@C-F300	91.7	4.59	7.8	47	0.59

KFe@C-MIL100 exhibits slightly higher methane selectivity. The activation periods of KFe@C vary between 0 to 50 h, with a trend toward longer activation for the catalysts with lower activity. Again, the catalyst with N- functionalization exhibits deactivation, however, to a much smaller extent compared to the unpromoted Fe@C-MIL101NH<sub>2</sub> (1.9% vs 8.9%). Remarkably, the KFe@C-MIL127 catalyst shows the highest methane selectivity combined with the highest value for alpha, implying some deviation from ideal ASF behaviour and suggesting the presence of Fe sites with enhanced hydrogenation activity. KFe@C-F300 combines the highest *FTY* with the lowest CH<sub>4</sub> selectivity while operating at very high conversion levels, indicating its performance does not suffer from higher local hydrogen concentrations due to limiting CO reactant depletion or diffusion limitations.

## Discussion

### Characterization of Fe@C catalysts

Key in this work was examining the influence of the MOFs on the Fe@C formation in terms of the C matrix properties and Fe nanoparticle size, as it would allow for the formulation of structure-activity relations to the Fischer-Tropsch synthesis. The porosity and surface area are very similar when transforming the values to per gram of C matrix. These results indicate a comparable pyrolysis behaviour, implying that the framework in itself does not have an effect on the resulting porosity, and that other factors like temperature and duration of pyrolysis influence the properties of the C matrix. These claims are supported by the limited porosity and surface area by pyrolysis of MIL-88A for just 1 h, obtaining a BET area of 115 m<sup>2</sup> g<sup>-1</sup>, only half of the value reported in this work<sup>43</sup>. The similar pyrolysis behaviour for the Fe@C catalysts was confirmed by analysing the degree of carbonization, calculated from C/O ratios of the C matrix, indicating one molecule of CO<sub>2</sub> is removed from the framework next to an additional O molecule, assumed to be in the form of a water molecule. In previous work, we showed that the structure collapse by initial decarboxylation is followed by carboxylate side reactions, supposedly forming anhydride species as intermediates towards more graphite-like structures<sup>16</sup>. Additionally, higher C/O ratios were found on the surface than in the bulk, suggesting that surface C is more prone to releasing O from its structure. The presence of graphitic shells on the surface of the Fe nanoparticles, witnessed in HR-TEM, suggest that Fe plays an important role in the carbonization process by scavenging O from the C matrix. Such C morphology control and graphitization have been illustrated previously in Fe-MOF pyrolysis<sup>44</sup>. These generalizations seem valid for Fe carboxylates, but extrapolation to non-carboxylate MOF with different metal-ligand interaction is speculative. The average Fe nanoparticle size obtained from the Fe-MOF pyrolysis is not a function of the Fe loading, but seems to be related to the structure and porosity of the original MOF precursor. A trend towards smaller Fe nanoparticles is visible with increasing

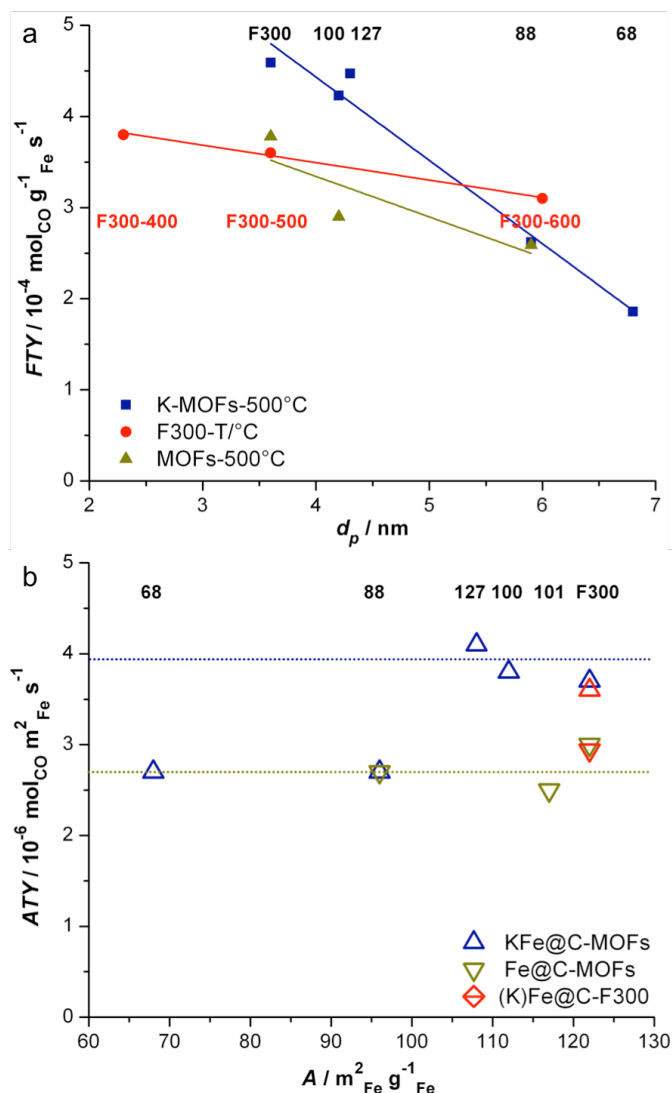


Figure 6. a) Correlation between Fe nanoparticle size and catalytic activity normalized for the Fe mass (*FTY*), including data from Fe@C-F300 synthesized at different temperatures<sup>16</sup> and b) catalytic activity normalized for the Fe surface area (*ATY*) of several Fe@C catalysts<sup>8</sup>.

surface area and pore volume (Figure S9). Shorter nearest-neighbour distances of Fe clusters may very well play a role in the formation of larger Fe nanoparticles, as is clearly observed for the highly contracted and non-porous MIL-88A, having an average nanoparticle size of 5.9 nm. An additional factor at play is the decomposition temperature, being the lowest for MIL-68 and -88A, forming the largest Fe nanoparticles.

### Catalytic testing

The activity of Fe@C catalysts displayed a linear dependence to the size of the Fe nanoparticles (Figure 6). For the unpromoted samples, the particle size effect on the activity was less pronounced than for the promoted samples, in line with previously reported *FTY* values for a similar range of particle sizes produced by pyrolysis of F300 Fe-BTC at different temperatures<sup>16</sup>. These findings indicate that particle size is the key factor in Fe@C catalyst design, and this effect is even more pronounced in the K-promoted samples. The surface specific

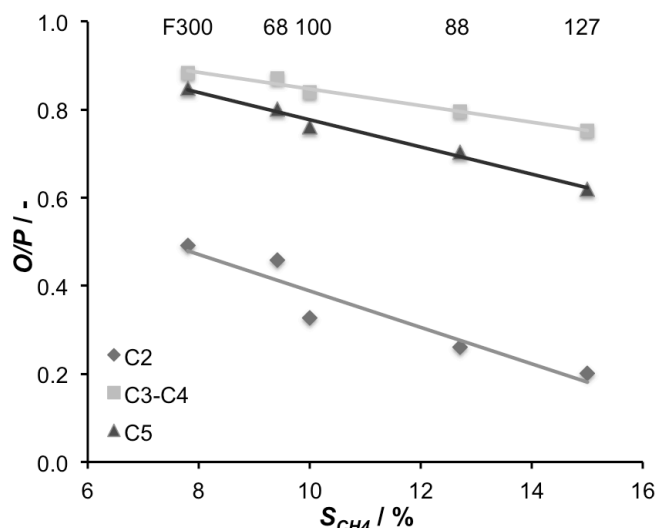


Figure 7. Correlation of the hydrogenation ability of KFe@C catalysts displaying olefin to paraffin ratio ( $O/P$ ) and methane selectivity ( $S_{CH_4}$ ).

activity, or areal time yield ( $ATY$ ), provides clearer insight into the relative catalytic activity of the different samples. All unpromoted Fe@C show similar performance, whereas higher  $ATY$  are obtained for the promoted catalysts (Figure 6). The exceptions to this trend are the KFe@C-MIL68 and -88, which display  $ATY$  similar to that of unpromoted catalysts. From these results, together with the identical  $O/P$  ratios ( $C_3$ - $C_4 = 0.8$  and  $C_5 = 0.7$  for both) and even slightly higher methane selectivity than that observed for the unpromoted Fe@C-MIL88, we conclude that K promotion in these samples is not as effective as in the other cases. Furthermore, we suspect that the lower Fe surface area of KFe@C-MIL68 results in K overpromotion, giving rise to some CO disproportionation ( $S_{CO_2} = 55\%$ )<sup>45</sup>. In general, the alkali promotion resulted in decreased hydrogenation ability of KFe@C catalysts, showing a linear correlation toward far higher  $O/P$  ratios, and additionally, providing much higher activity (Figure 7). To put into perspective, the productivity of lower olefins as chemicals precursors is maximized with the best KFe@C catalysts, obtaining 50-90% of olefins in the  $C_2$ - $C_5$  range with  $CO_2$ -free selectivity over 53% without showing deactivation after 80 h. As discussed, deactivation was only observed for N-functionalized Fe@C catalysts, although this apparent relationship seems somewhat counterintuitive. For example, in studies on Fe/CNT for use as FTS catalysts, N-functionalization is often used to enhance the anchoring of Fe particles in the CNTs, thus increasing their activity and stability<sup>46-47</sup>. Furthermore, the increased addition of N groups to the support often decreases the  $CH_4$  selectivity in FTS over these N-doped carbons<sup>48</sup>. Therefore, EDX mapping of large clusters of catalysts was performed on the samples that contained impurities in the XPS spectra (Table 5, Figure S10 and S11). EDX results confirmed the K loading obtained by ICP analysis and showed the high dispersion of the alkali, and additionally confirmed bulk impurities for KFe@C-MIL88, -100, -127 and -F300. The EDX analysis of KFe@C-MIL88 and -127 contained 0.5 and 1.0 wt% of highly dispersed Cl. The EDX mapping for

Table 5. Results of EDX mapping studies on KFe@C catalysts.

X/Fe mol%	KFe@C-MIL68	KFe@C-MIL88A	KFe@C-MIL100	KFe@C-MIL127	KFe@C-F300
K/Fe	2.10	2.18	1.57	1.73	1.97
Cl/Fe		2.34		4.79	
Cr/Fe			5.58		
Mo/Fe			2.40		
N/Fe				73.2	
S/Fe					0.85
Cu/Fe					0.85
Mn/Fe					1.55

KFe@C-MIL100 displayed that large amounts (4.9 wt% total) of Cr and Mo were located in agglomerates, most likely in the form of bulk metal oxides. Interestingly, the KFe@C-F300 catalyst with the highest activity and lowest  $CH_4$  selectivity contained Cu, Mn and S in amounts known as optimum for promoting FTS activity and selectivity<sup>41-42, 49-52</sup>. Minute amounts of S are reported to titrate the active sites for hydrogenation, increasing the  $O/P$  ratio and activity, but unaffected the  $\alpha$  value<sup>49-50</sup>. Additionally, increased activity from S promotion was shown by DFT calculations to originate from a decrease in the Fe-CO bond strength<sup>52</sup>. Cu is reported to increase the reduction of  $Fe_2O_3$  by a combination of textural and  $H_2$  spillover effects, and promotes the reaction rates in FTS and WGS<sup>41, 53</sup>. Apparently, it is the exact combination of the abovementioned promoters that distinguishes KFe@C-F300 as the best catalyst tested in this study.

## Conclusions

In the preparation of FTS catalysts through the MOF mediated synthesis approach, the structure and elementary composition of the MOF play a key role on the FTS activity and selectivity of the resulting Fe on C composites. On one hand, the exact composition of the linker seems to play a small role in the surface area of the resulting C matrix ( $S_{BET}$  between 570-670  $m^2 g^{-1}$ ). On the other hand, pore size distribution and average Fe particle size of the final catalysts are highly dependent on the original topology. All Fe@C samples prepared following this approach displayed outstanding activities in HT-FTS, especially after promotion with K ( $FTY$  in the range of 1.9-4.6  $\cdot 10^{-4} mol_{CO} g^{-1}_{Fe} s^{-1}$ ). The obtained activities correlate well with the surface of the Fe particles, though the  $ATY$  of KFe@C-MIL-68 and -88 revealed that K promotion did not improve their activity. When it comes to selectivity to short chain olefins and catalyst deactivation, our results highlight the importance of impurities and the presence of other heteroatoms in the original MOF precursor. The use of linkers containing N resulted in less stable catalysts, while an optimum final composition is obtained when the commercial Fe-BTC MOF is used as precursor. In addition to added K, the presence of traces of S, Mn and Cu, most likely originating from its synthesis conditions, result in a lower hydrogenation activity and decreased Fe-CO bond strength. The combined effects result in decreased methane selectivity, increased  $O/P$  ratio and increased activity. Altogether, our results further

demonstrate the complexity of FTS and the potential of commercial MOFs for the preparation of a new generation of catalysts able to fulfil most of the requirements of this challenging reaction.

## Experimental

### Synthesis

The Fe-based MOFs used in this research were commercially acquired from BASF (Basolite F300®) and from MOFTECH (MIL-68, MIL-88A, MIL-100, MIL-101-NH<sub>2</sub> and MIL-127). They were used without further purification in both the pyrolysis and characterization. Pyrolysis of the MOFs was performed in a quartz tubular reactor ( $L = 1.0\text{ m} \times \text{ID} = 5.0\text{ cm}$ ) located horizontally in a ceramic fiber oven (Carbolite, Sheffield) where between 50–100 mg of the MOF was placed in a ceramic crucible and subjected to heat treatment in a nitrogen atmosphere ( $150\text{ cm}^3\text{ min}^{-1}_{\text{STP}}$ , gas hourly space velocity  $4.5\text{ h}^{-1}$ ). The pyrolysis temperature was fixed at  $500\text{ }^\circ\text{C}$ , the ramp rate and dwell time were set to  $2\text{ }^\circ\text{C min}^{-1}$  and 8 h, respectively. Before exposure to ambient conditions each material was passivated at room temperature using a stream of 5 vol% O<sub>2</sub> in N<sub>2</sub> for 2 h. The synthesized catalysts are denoted herein as “Fe@C-X”, with X representing the MOF used as catalyst precursor. Incipient wetness impregnation (IWI) was carried out with a 50:50 v% methanol/water solution in which K<sub>2</sub>CO<sub>3</sub> was dissolved. The amount dissolved is determined by the iron loading of the sample with molar ratio K/Fe = 0.0226, aiming at 0.6 wt% of K loading. The IWI volume used is  $1.0\text{ cm}^3\text{ g}^{-1}$  and is pipetted onto the sample. After careful mixing, the sample is put in an ultrasonic bath for 90 min and dried in N<sub>2</sub> atmosphere for 4 h at  $250\text{ }^\circ\text{C}$ . K-promoted samples are denoted as KFe@C-X, where K is added to distinguish the promoted samples.

### Characterization

*Thermogravimetric analysis (TGA)* was performed on a Mettler Toledo TGA/SDTA1 with sample robot (TSO 801RO) and gas control (TSO 800GC1). The temperature was linearly increased from 25 to  $1000\text{ }^\circ\text{C}$  at a heating rate of  $5\text{ }^\circ\text{C min}^{-1}$  under air flow. The Fe loading of the carbon-matrix catalysts was calculated using the Fe<sub>2</sub>O<sub>3</sub> phase residual mass.

*Powder X-ray diffraction (PXRD)* was performed with a Bruker D8 Advance diffractometer in Bragg-Brentano geometry with Co K $\alpha$  radiation and a Lynxeye position sensitive detector. The slit used was a Divergence slit V12. The scatter screen height was 5 mm with 45 kV at 40 mA. Data was analysed by Bruker software Diffrac.EVA version 4.0.

*N<sub>2</sub>-physisorption* was performed on a Micromeritics Tristar II at 77 K to determine the textural properties of compounds. All samples were evacuated at  $175\text{ }^\circ\text{C}$  for 16 h prior to measurement. Data analysis was performed with Microactive software V3.00. The BET area was determined by direct fitting of points in the  $P/P_0 = 0.05\text{--}0.15$  domain, constraining the upper boundary of the relative pressure window using the

two-point BET method.<sup>54</sup> Total pore volume was measured at  $P/P_0 = 0.95$  where no inter-particle condensation occurred, the external surface area and microporous volume were determined by the *t*-method, obtaining a linear fit in the De Boer thickness of at least 10 data points.

*Elemental analysis* was carried out with inductively coupled plasma optical emission spectroscopy (ICP-OES) instrumentation. First, samples underwent destruction in a closed flask under high temperature and pressure. C was measured with a CHNOS-Analyzer from Elementar; Fe has been measured after an acidic destruction with an Analyst 200 AAS from Perkin Elmer. About 5 mg of sample was used per element measured.

*X-ray photoelectron spectroscopy (XPS)* measurements were performed on a K-alpha Thermo Fisher Scientific spectrometer using a monochromatic Al K $\alpha$  X-ray source. The measurements were carried out using point analysis with auto-height signal optimization, with each point having a spot size of 300 micron at ambient temperature and chamber pressure of about  $10^{-8}$  mbar. A flood gun was used for charge compensation. All the spectra measured were corrected by setting the reference binding energy of C1s at  $284.8 \pm 0.025\text{ eV}$ . The electron energy analyzer was operated with pass energy of 200 eV and 0.25 eV energy spacing for the survey spectrum, and pass energy of 50 eV and 0.1 eV energy spacing for the high-resolution spectrum was used. Each spectrum reported is the statistic average of 10 measured scans. The spectra were analyzed and processed using Thermo Advantage v5.903 software (Thermo Fisher Scientific). Smart background subtraction, derived from the Shirley background, was used over the peak width. By applying full width integration over the core-level signals and using tabulated atomic sensitivity factors (ASF), relative atomic contributions on the surface were calculated.

*Scanning electron microscope (SEM)* images and energy dispersive X-ray (EDX) spectra of the samples were recorded by a JEOL JSM-7500F field emission scanning electron microscope equipped with a Noran System Six spectral imaging system and a 30mm<sup>2</sup> Noran detector. For SEM, an acceleration of 5 kV was used with a spot size of 20–50 nm. For EDX, the acceleration was increased to 20 kV and scanning times of 5 min are used to determine chemical composition. Elemental mapping was performed with similar settings employing a mapping time of approximately 15 min.

*High-resolution transmission electron micrographs (HRTEM)* were collected on a JEOL model JEM-2010 working at 200 kV with a LaB<sub>6</sub> filament. It reaches a resolution between layers of 0.14 nm and between points of 0.25 nm. It is equipped with an Orius 831 camera from Gatan. Ethanol suspensions containing the samples were deposited onto a Au grid covered with lacey carbon and left to dry in air prior to measuring.

### Catalyst testing

The catalyst performance tests were conducted in the high-pressure reactor assembly module-I (HPRAM-I) system at the Dow Chemical Company. It consists of 48 reactors that can be

operated simultaneously at various process conditions, gas feed systems, exit modules with flow splitters, and gas chromatograph analyzers (Siemens Maxum-II). For activity testing, ~10 mg (20 mm<sup>3</sup>) of fresh catalyst with the particle size of 177–420 μm was diluted with 100 mm<sup>3</sup> SiC particles of similar size range. First, samples were activated *in situ* in a 90/10 vol% H<sub>2</sub>/He mixture at 425 °C for 3 h at 3 bar followed by cooling to 340 °C under N<sub>2</sub> flow at the same pressure. After increasing the pressure to the process set point of 20 bar, a 10 cm<sup>3</sup> min<sup>-1</sup><sub>STP</sub> flow consisting of CO 45 vol%, H<sub>2</sub> 45 vol% and He 10 vol% was introduced. These operating conditions are hereby referred to as high-temperature Fischer-Tropsch (HT-FTS) conditions. Catalytic activity is expressed as Fe time yield (FTY), defined as the number of moles of CO converted to hydrocarbons per gram of Fe per second, and as areal time yield (ATY), moles of CO converted to hydrocarbons per surface area of Fe particles per second. CO conversion and carbon selectivity are defined by equations S1 and S2, respectively, where  $X_{CO}$  stands for CO conversion,  $F$  indicates the molar flow,  $S$  is the carbon selectivity towards a product with  $n$  carbon atoms and  $y$  is the molar fraction of a hydrocarbon  $C_n$ .

$$X_{CO} = \left( 1 - \frac{C_{He,d,R} \cdot C_{CO,d,R}}{C_{He,d,blk} \cdot C_{CO,d,blk}} \right) \cdot 100\% \quad (S1)$$

where  $C_{He,d,blk}$ ,  $C_{He,d,R}$ ,  $C_{CO,d,blk}$ ,  $C_{CO,d,R}$  are the concentrations determined by GC analysis of He in the blank, He in the diluted reactor effluent, CO in the blank, and CO in the diluted reactor effluent, respectively.

$$S_{C_n} = \frac{n \cdot \left( \frac{C_{C_n,d,R}}{C_{He,d,R}} \right)}{\left( \frac{C_{CO,d,blk}}{C_{He,d,blk}} - \frac{C_{CO,d,R}}{C_{He,d,R}} \right)} \cdot 100\% \quad (S2)$$

where  $C_{C_n,d,R}$  is the concentration the diluted reactor effluent determined by GC analysis of a product with  $n$  carbon atoms.

## Acknowledgements

We would like to thank Harrie Jansma, Bart van der Linden, Kevin Mouthaan, Willy Rook, Bart Boshuizen, Ben Norder and Duco Bosma for the technical support during this project.

## Notes and references

‡ Limited data was available for MIL-101-NH<sub>2</sub> due to practical issues between characterization, pyrolysis and catalytic testing.

- Schulz, H., *Appl. Catal.*, A **1999**, *186* (1–2), 3–12.
- Stranges, A. N., A history of the fischer-tropsch synthesis in Germany 1926–45. In *Studies in Surface Science and Catalysis*, Davis, B. H.; Ocelli, M. L., Eds. Elsevier: Amsterdam, 2007; Vol. 163, pp 1–27.
- Dry, M. E., *Catal. Today* **2002**, *71* (3–4), 227–241.
- Rostrup-Nielsen, J. R., *Catal. Today* **1993**, *18* (4), 305–324.

- Rostrup-Nielsen, J. R., *Catal. Today* **1994**, *21* (2–3), 257–267.
- Steynberg, A. P.; Espinoza, R. L.; Jager, B.; Vosloo, A. C., *Appl. Catal.*, A **1999**, *186* (1–2), 41–54.
- Gascon, J.; Corma, A.; Kapteijn, F.; Lladrés i Xamena, F. X., *ACS Catal.* **2013**, *4* (2), 361–378.
- Santos, V. P.; Wezendonk, T. A.; Jaén, J. J. D.; Dugulan, A. I.; Nasalevich, M. A.; Islam, H.-U.; Chojecki, A.; Sartipi, S.; Sun, X.; Hakeem, A. A.; Koeken, A. C. J.; Ruitenbeek, M.; Davidian, T.; Meima, G. R.; Sankar, G.; Kapteijn, F.; Makkee, M.; Gascon, J., *Nat Commun* **2015**, *6*, 1–8.
- Chen, Y.-Z.; Wang, C.; Wu, Z.-Y.; Xiong, Y.; Xu, Q.; Yu, S.-H.; Jiang, H.-L., *Adv. Mater.* **2015**, *27* (34), 5010–5016.
- Jiang, H.-L.; Liu, B.; Lan, Y.-Q.; Kuratani, K.; Akita, T.; Shioyama, H.; Zong, F.; Xu, Q., *J. Am. Chem. Soc.* **2011**, *133* (31), 11854–11857.
- Kim, T. K.; Lee, K. J.; Cheon, J. Y.; Lee, J. H.; Joo, S. H.; Moon, H. R., *J. Am. Chem. Soc.* **2013**, *135* (24), 8940–8946.
- Lee, J. H.; Moon, B.; Kim, T. K.; Jeoung, S.; Moon, H. R., *Dalton Transactions* **2015**, *44* (34), 15130–15134.
- Lee, K. J.; Kim, T.-H.; Kim, T. K.; Lee, J. H.; Song, H.-K.; Moon, H. R., *J. Mater. Chem. A* **2014**, *2* (35), 14393–14400.
- Shen, K.; Chen, X.; Chen, J.; Li, Y., *ACS Catal.* **2016**, *6* (9), 5887–5903.
- An, B.; Cheng, K.; Wang, C.; Wang, Y.; Lin, W., *ACS Catal.* **2016**, *6* (6), 3610–3618.
- Wezendonk, T. A.; Santos, V. P.; Nasalevich, M. A.; Warringa, Q. S. E.; Dugulan, A. I.; Chojecki, A.; Koeken, A. C. J.; Ruitenbeek, M.; Meima, G.; Islam, H.-U.; Sankar, G.; Makkee, M.; Kapteijn, F.; Gascon, J., *ACS Catal.* **2016**, *6* (5), 3236–3247.
- Crawford, D.; Casaban, J.; Haydon, R.; Giri, N.; McNally, T.; James, S. L., *Chem. Sci.* **2015**, *6* (3), 1645–1649.
- Crawford, D. E.; Casaban, J., *Adv. Mater.* **2016**, *28* (27), 5747–5754.
- Taddei, M.; Steitz, D. A.; van Bokhoven, J. A.; Ranocchiari, M., *Chemistry – A European Journal* **2016**, *22* (10), 3245–3249.
- Wilmer, C. E.; Leaf, M.; Lee, C. Y.; Farha, O. K.; Hauser, B. G.; Hupp, J. T.; Snurr, R. Q., *Nat Chem* **2012**, *4* (2), 83–89.
- Fateeva, A.; Horcajada, P.; Devic, T.; Serre, C.; Marrot, J.; Grenèche, J.-M.; Morcrette, M.; Tarascon, J.-M.; Maurin, G.; Férey, G., *Eur. J. Inorg. Chem.* **2010**, *2010* (24), 3789–3794.
- Volklinger, C.; Meddouri, M.; Loiseau, T.; Guillou, N.; Marrot, J.; Férey, G.; Haouas, M.; Taulelle, F.; Audebrand, N.; Latroche, M., *Inorg. Chem.* **2008**, *47* (24), 11892–11901.
- Serre, C.; Mellot-Draznieks, C.; Surblé, S.; Audebrand, N.; Filinchuk, Y.; Férey, G., *Science* **2007**, *315* (5820), 1828.
- Mellot-Draznieks, C.; Serre, C.; Surblé, S.; Audebrand, N.; Férey, G., *J. Am. Chem. Soc.* **2005**, *127* (46), 16273–16278.
- Serre, C.; Millange, F.; Surblé, S.; Férey, G., *Angew. Chem. Int. Ed.* **2004**, *43* (46), 6285–6289.
- Surble, S.; Serre, C.; Mellot-Draznieks, C.; Millange, F.; Férey, G., *Chem. Commun.* **2006**, (3), 284–286.
- Férey, G.; Serre, C.; Mellot-Draznieks, C.; Millange, F.; Surblé, S.; Dutour, J.; Margiolaki, I., *Angew. Chem. Int. Ed.* **2004**, *43* (46), 6296–6301.
- Horcajada, P.; Surble, S.; Serre, C.; Hong, D.-Y.; Seo, Y.-K.; Chang, J.-S.; Grenèche, J.-M.; Margiolaki, I.; Férey, G., *Chem. Commun.* **2007**, (27), 2820–2822.
- Volklinger, C.; Popov, D.; Loiseau, T.; Férey, G.; Burghammer, M.; Riekel, C.; Haouas, M.; Taulelle, F., *Chem. Mater.* **2009**, *21* (24), 5695–5697.
- Bauer, S.; Serre, C.; Devic, T.; Horcajada, P.; Marrot, J.; Férey, G.; Stock, N., *Inorg. Chem.* **2008**, *47* (17), 7568–7576.
- Férey, G.; Mellot-Draznieks, C.; Serre, C.; Millange, F.; Dutour, J.; Surblé, S.; Margiolaki, I., *Science* **2005**, *309* (5743), 2040.
- Taylor-Pashow, K. M. L.; Rocca, J. D.; Xie, Z.; Tran, S.; Lin, W., *J. Am. Chem. Soc.* **2009**, *131* (40), 14261–14263.

- 33 Chevreau, H.; Permyakova, A.; Nouar, F.; Fabry, P.; Livage, C.; Ragon, F.; Garcia-Marquez, A.; Devic, T.; Steunou, N.; Serre, C.; Horcajada, P., *CrystEngComm* **2016**, *18* (22), 4094-4101.
- 34 Cunha, D.; Ben Yahia, M.; Hall, S.; Miller, S. R.; Chevreau, H.; Elkaim, E.; Maurin, G.; Horcajada, P.; Serre, C., *Chem. Mater.* **2013**, *25* (14), 2767-2776.
- 35 Liu, Y.; Eubank, J. F.; Cairns, A. J.; Eckert, J.; Kravtsov, V. C.; Luebke, R.; Eddaoudi, M., *Angew. Chem. Int. Ed.* **2007**, *46* (18), 3278-3283.
- 36 Biesinger, M. C.; Payne, B. P.; Grosvenor, A. P.; Lau, L. W. M.; Gerson, A. R.; Smart, R. S. C., *Appl. Surf. Sci.* **2011**, *257* (7), 2717-2730.
- 37 Kapteijn, F.; Moulijn, J. A.; Matzner, S.; Boehm, H. P., *Carbon* **1999**, *37* (7), 1143-1150.
- 38 Pels, J. R.; Kapteijn, F.; Moulijn, J. A.; Zhu, Q.; Thomas, K. M., *Carbon* **1995**, *33* (11), 1641-1653.
- 39 Chaumette, P.; Verdon, C.; Boucot, P., *Top. Catal.* **1995**, *2* (1), 301-311.
- 40 Mills, G. A.; Steffgen, F. W., *Catalysis Reviews* **1974**, *8* (1), 159-210.
- 41 Bukur, D. B.; Mukesh, D.; Patel, S. A., *Industrial & Engineering Chemistry Research* **1990**, *29* (2), 194-204.
- 42 Li, S.; Li, A.; Krishnamoorthy, S.; Iglesia, E., *Catal. Lett.* **2001**, *77* (4), 197-205.
- 43 Li, Y.; Zhou, Y.-X.; Ma, X.; Jiang, H.-L., *Chem. Commun.* **2016**, *52* (22), 4199-4202.
- 44 Li, Q.; Xu, P.; Gao, W.; Ma, S.; Zhang, G.; Cao, R.; Cho, J.; Wang, H.-L.; Wu, G., *Adv. Mater.* **2014**, *26* (9), 1378-1386.
- 45 Kapteijn, F.; Moulijn, J. A., *J. Chem. Soc., Chem. Commun.* **1984**, (5), 278-279.
- 46 Lu, J.; Yang, L.; Xu, B.; Wu, Q.; Zhang, D.; Yuan, S.; Zhai, Y.; Wang, X.; Fan, Y.; Hu, Z., *ACS Catal.* **2014**, *4* (2), 613-621.
- 47 Schulte, H. J.; Graf, B.; Xia, W.; Muhler, M., *ChemCatChem* **2012**, *4* (3), 350-355.
- 48 Xiong, H.; Moyo, M.; Motchelaho, M. A.; Tetana, Z. N.; Dube, S. M. A.; Jewell, L. L.; Coville, N. J., *J. Catal.* **2014**, *311*, 80-87.
- 49 Bromfield, T. C.; Coville, N. J., *Appl. Catal., A* **1999**, *186* (1-2), 297-307.
- 50 Torres Galvis, H. M.; Koeken, A. C. J.; Bitter, J. H.; Davidian, T.; Ruitenbeek, M.; Dugulan, A. I.; de Jong, K. P., *J. Catal.* **2013**, *303*, 22-30.
- 51 van Dijk, W. L.; Niemantsverdriet, J. W.; van der Kraan, A. M.; van der Baan, H. S., *Applied Catalysis* **1982**, *2* (4), 273-288.
- 52 Cheng, J.; Hu, P.; Ellis, P.; French, S.; Kelly, G.; Lok, C. M., *J. Phys. Chem. C* **2010**, *114* (2), 1085-1093.
- 53 de Smit, E.; de Groot, F. M. F.; Blume, R.; Havecker, M.; Knop-Gericke, A.; Weckhuysen, B. M., *PCCP* **2010**, *12* (3), 667-680.
- 54 De Lange, M. F.; Vlugt, T. J. H.; Gascon, J.; Kapteijn, F., *Microporous Mesoporous Mater.* **2014**, *200*, 199-215.